Soft Matter

PAPER

View Article Online
View Journal | View Issue

Cite this: *Soft Matter*, 2022, **18**, 5312

Self-sustained three-dimensional beating of a model eukaryotic flagellum†

Bhargav Rallabandi, *[a] Qixuan Wang *[b] and Mykhailo Potomkin [b]

Flagella and cilia are common features of a wide variety of biological cells and play important roles in locomotion and feeding at the microscale. The beating of flagella is controlled by molecular motors that exert forces along the length of the flagellum and are regulated by a feedback mechanism coupled to the flagella deformation. We develop a three-dimensional (3D) flagellum beating model based on sliding-controlled motor feedback, accounting for both bending and twist, as well as differential bending resistances along and orthogonal to the major bending plane of the flagellum. We show that beating is generated and sustained spontaneously for a sufficiently high motor activity through an instability mechanism. Isotropic bending rigidities in the flagellum lead to 3D helical beating patterns. By contrast, anisotropic flagella present a rich variety of wave-like beating dynamics, including both 3D beating patterns as well as planar beating patterns. We show that the ability to generate nearly planar beating despite the 3D beating machinery requires only a modest degree of bending anisotropy, and is a feature observed in many eukaryotic flagella such as mammalian spermatozoa.

Received 23rd April 2022,
Accepted 19th June 2022

DOI: 10.1039/d2sm00514j

rsc.li/soft-matter-journal

1 Introduction

Many biological microorganisms and motile cells rely on the coordinated beating of their cilia or flagella to swim or feed in a fluid environment. Examples include spermatozoa and *C. reinhardtii*, among several others. Besides their important roles in the self-propulsion, cilia and flagella also play critical roles in physiological process in other organisms. Several organisms additionally use arrays of collectively beating cilia to pump fluid and filter out undesired particles. For example, such arrays are responsible for clearance mechanisms of the respiratory tract.[1,2] The mechanisms governing the beating of cilia and flagella, as well as the underlying routes to their synchronization, have been a topic of considerable interest.[3–6]

The core of an eukaryotic flagellum or cilium (below we consider flagella only) is the axoneme, a cylindrical skeleton structure consisting of nine microtubule doublets on the circumference and a pair of single microtubules at the center – the "9 + 2" structure;[7–9] see Fig. 1. This structure is ubiquitous for eukaryotes, and has evolved with little variation over the last billion years.[10–12] Each circumferential doublet comprises two distinct microtubules: an A-tubule, which has a circular cross-section and a B-tubule, whose cross-section is an incomplete circle attached to the A-tubule (Fig. 1); see section 19.4 in ref. 13. The robustness of the axoneme structure and transmission of signals from the central pair to circumference is maintained by radial spokes, T-shaped macromolecular complexes whose thin ends are anchored to the circumferential doublets and whose wide ends project towards the central pair of microtubules.[14] Adjacent circumferential doublets are connected by linkers composed of the protein nexin.

The beating of a eukaryotic flagellum is powered by dynein molecular motors.[15] Dyneins are spaced at almost equal intervals between circumference doublets along the entire length of

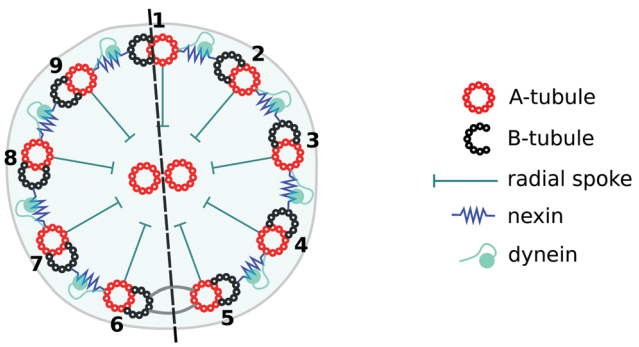

Fig. 1 Schematic of axoneme – a cross-section of flagella, as seen from the base looking towards the tip, with circumference doublets labeled from 1 to 9. A "bridge" between doublets 5 and 6 (two curved gray segments) defines the major bending plane (dashed line).

[a] *Department of Mechanical Engineering, University of California, Riverside, CA 92521, USA. E-mail: bhargav@engr.ucr.edu*
[b] *Department of Mathematics, University of California, Riverside, CA 92521, USA. E-mail: qixuanw@ucr.edu*

† Electronic supplementary information (ESI) available. See DOI: https://doi.org/10.1039/d2sm00514j

the flagellum and are anchored to A-tubules, and directed towards the closest adjacent B-tubules, to which they may bind; Fig. 1. When bound and also activated by hydrolysis of adenosine triphosphate (ATP), dyneins generate active sliding forces (by "walking" along the B-tubule and pulling it towards the tip) which in turn causes the flagellum to bend[7–9] through the surrounding fluid. Synchronization of these motors then results in beating. Flagella are typically several tens of microns long and move at a few microns per second, so inertia has a mostly negligible effect on the beating dynamics.

How the individual dynein motors spontaneously synchronize their activity and sliding force generation, necessary to generate the regular flagellum beating needed for steady swimming, has been the focus of many modeling and numerical studies. Several mechanisms have been proposed to explain the highly cooperative behavior of dyneins, though which ones are most biophysically relevant remains a topic of debate. In ref. 16–18, it was conjectured that dynein activity is regulated by the longitudinal curvature of the axoneme structure. In ref. 19 and 20, a geometrical clutch theory was developed in which dynein attachment/detachment activity depends on inter-doublet distance. In ref. 18 and 21–25 a sliding-control model was developed, in which it was hypothesized that dynein attachment/detachment results from sliding forces acting parallel to the long axis of the microtubule doublets. In these models dyneins tend to split locally in two opposing groups such that dyneins on one side of axoneme build-up sliding forces leading to detachment of dyneins on the other side. This "tug-of-war" (see, *e.g.*, Fig. 1 in ref. 25) results in generation of self-organized oscillations of axoneme.

For many protozoa (single celled eukaryotes), a pair of adjacent circumference doublets (typically doublets 5 and 6; see Fig. 1) are connected by a relatively stiff "bridge".[26] This defines a major bending plane (dashed line in Fig. 1) through which the flagellum can bend with relative ease, while bending through the orthogonal plane is relatively stiff. This leads naturally to the notion of 2D wave propagation along the entire length of axoneme, controlled by a coupled dynamics of two effective filaments representing the two competing sides.[18,24,27–29] A description of dynein activity in the framework of a 2D two-filament model was introduced and analyzed in terms of buckling instability in ref. 27 and further developed to include important nonlinear effects in ref. 28 and 29.

A growing number of experiments show that observed beating patterns of flagellated cells are generally three-dimensional, for example in sperm[30,31] and in *Chlamydomonas*.[32] Three-dimensional flagellum models[18,33,34] have either focused on linearized dynamics or have not investigated the feedback of flagellum kinematics to motor kinetics.

Based on these works, we develop here a 3D computational model of eukaryotic flagellum in which the dynein activity is coupled to an explicit description of "9 + 2" structure that allows both bending and twist of the flagellum. Notably, we also model the effect of a "5–6 bridge" by introducing two distinct bending rigidities, B_1 and $B_2 \leq B_1$, which quantify differential resistance to bending orthogonal to and along the major bending plane, respectively. In this way, we use equal bending rigidities $B_1 = B_2$ to model an isotropic flagellum with no "bridge" between doublets 5 and 6. By varying the relative magnitudes of B_1 and B_2 we investigate how the breaking of bending isotropy by a "bridge" qualitatively and quantitatively affects the beating dynamics.

In Section 2, we first develop a 3D beating model that couples motor kinetics and the deformation of the flagellum. We investigate numerically in Section 3 how varying system parameters (dynein activity, bending rigidities, *etc.*) leads to self-sustained beating dynamics, including the emergence of instability with the transition to steady wave propagations along the flagellum, switching from planar beating to 3D, and changing wave propagation direction, *i.e.*, retrograde (from the tip to base) *vs.* anterograde (from the base to tip). We then use a linearized analysis to show how the onset of instability is qualitatively modified by even a slight bending anisotropy of the flagellum, before concluding in Section 4.

2 Model

We model a flagellum as a slender body with a circular cross-section of radius a and length $L \gg a$; see Fig. 2. The flagellum's centerline position is $\mathbf{x}(s,t)$ where $s \in [0,L]$ is the arc length. The unit vector tangent to the centerline is $\mathbf{d}(s,t) = \partial\mathbf{x}/\partial s$. To describe the geometry of the flexible flagellum we introduce a "material frame" or local Lagrangian frame given by an orthonormal basis $(\mathbf{e}_1(s,t), \mathbf{e}_2(s,t), \mathbf{d}(s,t))$. The material frame follows deformations of the flagellum, so that the position $\mathbf{x}(s,t) + x_1\mathbf{e}_1(s,t) + x_2\mathbf{e}_2(s,t)$ follows a material point for all t, for fixed (material quantities) s, x_1, and x_2. The set of orthonormal basis vectors $(\mathbf{e}_1, \mathbf{e}_2, \mathbf{d})$ coupled with centerline $\mathbf{x}(s,t)$ is often called the Cosserat curve (or rod) model.[35,36] Derivatives of the basis along the arclength define rotation angles $\phi_1(s,t)$, $\phi_1(s,t)$, and $\phi_3(s,t)$ according to[35]

$$\partial_s\mathbf{e}_1 = \partial_s\phi_3\mathbf{e}_2 - \partial_s\phi_2\mathbf{d}, \quad (1a)$$

$$\partial_s\mathbf{e}_2 = -\partial_s\phi_3\mathbf{e}_1 + \partial_s\phi_1\mathbf{d}, \quad (1b)$$

$$\partial_s\mathbf{d} = \partial_s\phi_2\mathbf{e}_1 - \partial_s\phi_1\mathbf{e}_2. \quad (1c)$$

The angles ϕ_1 and ϕ_2 quantify rotations about $\mathbf{e}_1$ and $\mathbf{e}_2$ axes, respectively; $\partial_s\phi_1$ and $\partial_s\phi_2$ are curvatures associated with bending of the flagellum. Note that $\partial_s\phi_2$ corresponds to deformation through the major bending plane; Fig. 2B. The angle ϕ_3

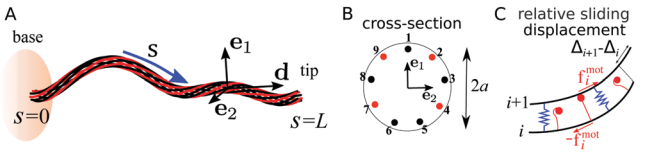

Fig. 2 Model of flagellum. Panel (A): A slender body (axoneme) composed of nine filaments (circumference doublets). Panel (B): A model flagellum's cross-section (*cf.* Fig. 1) as seen from the base looking toward the tip, rotated so that filament 1 is on the top. Panel (C): Relative sliding of two adjacent filaments (black solid line), nexins are represented by blue springs, and dynein motors are depicted as red straight segments with a head (active) and as curved segments (passive).

quantifies rotation about the tangent $\mathbf{d}$, and $\partial_s\phi_3$ quantifies the twisting of the flagellum.[35] Analogous relations to (1) apply when the s-derivatives are replaced by time derivatives.

We now define $\mathbf{F}(s,t)$ and $\mathbf{M}(s,t)$ as the internal force and moment exerted by the $(s,L]$ section of the flagellum on the $[0,s]$ section. A viscous force per length $\mathbf{f}_v(s,t)$ resists the motion of the flagellum as it sweeps through the fluid, and a viscous moment per length $\mathbf{m}_v(s,t)$ resists twisting. Inertia is typically negligible at the microscale, so the conservation of linear and angular momenta of the flagellum reduce to the local force and torque balances[35]

$$\partial_s\mathbf{F} + \mathbf{f}_v = \mathbf{0}, \tag{2a}$$

$$\partial_s\mathbf{M} + \mathbf{d} \times \mathbf{F} + \mathbf{m}_v = \mathbf{0}. \tag{2b}$$

Introducing the centerline velocity $\mathbf{v}(s,t) = \partial_t\mathbf{x} = \int_0^s \partial_t\mathbf{d}(u,t)\mathrm{d}u$, we approximate the viscous force by local resistive-force theory[37–40] as $\mathbf{f}_v = -\mathbf{R}\cdot\mathbf{v}$, where $\mathbf{R} = 8\pi\eta\xi_\perp\left(\mathbf{I} - \frac{\xi_\perp - \xi_\parallel}{\xi_\perp}\mathbf{dd}\right)$ is a local resistance tensor ($\mathbf{I}$ is the identity). Here, η is the dynamic viscosity of the surrounding fluid, and $\xi_\perp = (2\log\Lambda + 1)^{-1}$ and $\xi_\parallel = \frac{1}{2}(2\log\Lambda - 1)^{-1}$ are dimensionless resistance coefficients, with $\Lambda = L/a \gg 1$ (see, *e.g.*, eqn (8-178) and (8-179) of ref. 41). The viscous moment per length is similarly approximated as $\mathbf{m}_v = -2\pi a^2\eta\partial_t\phi_3\mathbf{d}$ (p. 49 of ref. 42). Following ref. 27–29, the internal moment $\mathbf{M}(s,t)$ comprises two components:

$$\mathbf{M} = \mathbf{M}^{\mathrm{bend}} + \mathbf{M}^{\mathrm{slide}}. \tag{3}$$

Here, $\mathbf{M}^{\mathrm{bend}} = B_1\partial_s\phi_1\mathbf{e}_1 + B_2\partial_s\phi_2\mathbf{e}_2 + J\partial_s\phi_3\mathbf{d}$ is the sum of the bending moment with stiffness coefficients are B_1 and B_2, and a twist moment associated with a stiffness J. The sliding moment $\mathbf{M}^{\mathrm{slide}} = \sum_{i=1}^{N}\mathbf{r}_i \times \mathbf{F}_i^{\mathrm{slide}}$ is exerted by the $(s,L]$ section of the flagellum on the $[0,s]$ section due to sliding of the axoneme circumference doublets (filaments 1 to 9 in Fig. 2) with respect to each other. Observe that a 5–6 bridge makes rotation about $\mathbf{e}_1$ "stiffer" than that about $\mathbf{e}_2$ (Fig. 1 and 2B), so we expect $B_1 > B_2$. Indeed, the "9 + 2" structure was modeled in ref. 43 experimentally with wooden staves and dowels instead of microtubule doublets and radial spokes, gluing together staves corresponding to doublet 5 and 6 to replicate the bridge effect, finding that $B_1/B_2 \approx 2.6$.

The sliding force $\mathbf{F}_i^{\mathrm{slide}}$ on each filament is determined by the dynamics of nexins and dynein motors. To model it we first describe the geometry of flagellum axoneme which comprises $N = 9$ filaments arranged around the centerline. We express the position of a point on filament i at a section s as

$$\mathbf{x}_i(s,t) = \mathbf{x}(s,t) + \mathbf{r}_i(s,t),$$

where

$$\mathbf{r}_i(s,t) = a(\mathbf{e}_1(s,t)\cos\theta_i + \mathbf{e}_2(s,t)\sin\theta_i), \quad i = 1,\ldots,N. \tag{4}$$

Here, $\theta_i = 2\pi(i-1)/N$ is an angle (internal to the flagellum) measured in the cross-sectional plane and is a material quantity attached to filament i. The arclength of filament i from the base up to a cross-section s is then $s_i(s,t) \equiv \int_0^s \partial_u|\mathbf{x}_i(u)|\mathrm{d}u$. The sliding displacement of filament i relative to the centerline is therefore

$$\Delta_i(s,t) = s - s_i(s,t) \approx a(\phi_2(s,t)\cos\theta_i - \phi_1(s,t)\sin\theta_i) \tag{5}$$

up to terms quadratic in ϕ_i, where we have used the relations (1).

We model the nexin linkers as linear springs of stiffness K that are distributed along the length of filaments. These springs connect neighboring filaments and exert forces in the $\pm\mathbf{d}$ directions to restore relative sliding displacements between neighbors, see Fig. 2C. The restoring spring force per length on filament i is therefore $\mathbf{f}_i^{\mathrm{spr}} = -K(\Delta_i - \Delta_{i-1})\mathbf{d} - K(\Delta_i - \Delta_{i+1})\mathbf{d}$. In addition, dynein motors are bound to each filament i at a mean number density per length ρ (assumed constant). A fraction $n_i(s,t)$ of these motors are engaged (that is, bound to filament $i+1$) and pull filament i towards the base ($s = 0$) and filament $i+1$ towards the tip ($s = L$) of the flagellum.[44–47] Denoting the load per motor on filament i by W_i, the active force exerted on filament i by its motors is $-\rho n_i W_i\mathbf{d}$; the same motors exert an opposite force of the same magnitude on filament $i+1$. Accounting for the motors engaging filament i with both its neighbors, the net active sliding force per length on filament i is $\mathbf{f}_i^{\mathrm{mot}} = \rho(W_{i-1}n_{i-1} - W_i n_i)\mathbf{d}$. Thus, the internal sliding force per length on filament i is the sum of a passive component due to nexin springs and an active component resulting from dynein motors,

$$\mathbf{f}_i(s,t) = \{K(\Delta_{i-1} - 2\Delta_i + \Delta_{i+1}) - \rho(W_i n_i - W_{i-1}n_{i-1})\}\mathbf{d}. \tag{6}$$

The sliding force exerted by the $(s,L]$ part of a filament on the $[0,s]$ part is therefore[27,28]

$$\mathbf{F}_i^{\mathrm{slide}}(s,t) = \int_s^L \mathbf{f}_i(u,t)\mathrm{d}u. \tag{7}$$

Observe that the resultant sliding force at a section s vanishes identically, $\left(\sum_{i=1}^{N}\mathbf{F}_i^{\mathrm{slide}} = \mathbf{0}\right)$, even though the resultant sliding moment $\left(\mathbf{M}^{\mathrm{slide}} = \sum_{i=1}^{N}\mathbf{r}_i \times \mathbf{F}_i^{\mathrm{slide}}\right)$ is generally nonzero.

Finally, motor kinetics describe the spatio-temporal evolution of the motor fractions n_i and the load per motor W_i. As noted earlier, motors on filament i move filament $i+1$ towards the tip and filament i towards the base with relative velocity $v_i = \partial_t(\Delta_{i+1} - \Delta_i)$. The load carried by motors on filament i decreases with this sliding velocity.[48] Following previous work,[27,48] we assume that this dependence is linear, so that

$$W_i = F_0(1 - v_i/v_0) = F_0(1 - \partial_t(\Delta_{i+1} - \Delta_i)/v_0), \tag{8}$$

where F_0 is the load at stall and v_0 is the zero-load velocity. Motor kinetics on each filament i are modeled by

$$\partial_t n_i = k_b(1 - n_i) - k_u n_i \exp\{W_i/F_c\} + \nu_i(s,t). \tag{9}$$

The first term corresponds to binding and the second term to unbinding, with rate constants k_b and k_u, respectively. The term $\nu_i(s,t)$ accounts for biochemical noise in the kinetics through a white noise that is spatially and temporally decorrelated.

The exponential models the rapid unbinding of motors when the motor load W_i exceeds a critical value F_c. The above description accounts for the bending elasticity of the flagellum, viscous forces and torques as well as the internal forces and torques related to the sliding of the flagellum, which in turn are driven by (and coupled to) motor kinetics.

We now make several simplifications and approximations. First, we eliminate the velocity $\mathbf{v}$ from (2a) by taking an s-derivative, and noting that $\partial_s\mathbf{v} = \partial_t\mathbf{d}$. Then, writing the sliding moment in terms of $\mathbf{F}_i^{\text{slide}}$ yields (ESI†)

$$\partial_s{}^2\mathbf{F} - \partial_s\mathbf{R}\cdot\mathbf{R}^{-1}\cdot\partial_s\mathbf{F} = \mathbf{R}\cdot\partial_t\mathbf{d} \tag{10a}$$

$$\partial_s\mathbf{M}^{\text{bend}} + \mathbf{d}\times\mathbf{F} + \mathbf{m}_{\text{v}} - \mathbf{m}^{\text{slide}} + \sum_{i=1}^{N}\partial_s\mathbf{r}_i\times\mathbf{F}_i^{\text{slide}} = \mathbf{0}, \tag{10b}$$

where

$$\mathbf{m}^{\text{slide}}(s,t) = \sum_{i=1}^{N}\mathbf{r}_i\times\mathbf{f}_i(s,t). \tag{10c}$$

The last two terms in (10b) together constitute $\partial_s\mathbf{M}^{\text{slide}}$. The quantity $\mathbf{m}^{\text{slide}}$ can be interpreted as the internal sliding moment per length and depends locally on $\mathbf{f}_i$, scaling linearly with the rotation angles ϕ_j for small rotations. By contrast, the term in (10b) involving $\mathbf{F}_i^{\text{slide}}$ depends nonlocally on $\mathbf{f}_i$ [*cf.* (7)] and scales quadratically with ϕ_j. We will retain only the local contribution below, mirroring the local theory used for viscous forces and torques.

Finally, we treat θ as continuous to homogenize the 9-filament structure. Then, the sliding displacement $\Delta_i(s,t)$ is replaced by the continuous function of θ,

$$\Delta(\theta,s,t) = a(\phi_2(s,t)\cos\theta - \phi_1(s,t)\sin\theta). \tag{11}$$

We define a sliding force per surface area $\sigma_i = \mathbf{f}_i/(a\delta\theta)$. Using (6) and approximating differences between neighboring filaments in terms of derivatives in θ, the continuous analog of σ_i is

$$\sigma(\theta,s,t) = \frac{1}{a}\big(K\delta\theta\partial_\theta{}^2\Delta - \rho\partial_\theta(Wn)\big)\mathbf{d}. \tag{12}$$

The sliding moment per length then becomes [*cf.* (10b)]

$$\begin{aligned}\mathbf{m}^{\text{slide}} &= \int_0^{2\pi}\mathbf{r}(\theta,s,t)\times\boldsymbol{\sigma}(\theta,s,t)a\mathrm{d}\theta = \frac{2\pi^2Ka^2}{N}(\phi_1\mathbf{e}_1+\phi_2\mathbf{e}_2)\\ &+\int_0^{2\pi}\rho aWn(\mathbf{e}_1\cos\theta+\mathbf{e}_2\sin\theta)\mathrm{d}\theta,\end{aligned} \tag{13}$$

The active motor fraction and motor load are similarly mapped to continuous functions of θ.

All physical parameters of the model are listed in Table 1. As noted earlier, the ''5–6 bridge'' favors bending about the $\mathbf{e}_2$ axis over that about the $\mathbf{e}_1$ axis, so $B_2 \le B_1$. We non-dimensionalize the problem by scaling lengths with the flagellum length L, time by the motor kinetic timescale $\tau_0 = (k_b + k_u)^{-1}$,[27,28] and the force by B_2/L^2. This choice of scales identifies several dimensionless parameters that are defined in Table 2. We then project the force and torque balances onto the basis ($\mathbf{e}_1$, $\mathbf{e}_2$, $\mathbf{d}$). This yields a system of partial differential equations for ϕ_1, ϕ_2, ϕ_3, F_1, F_2, F_3 and n,

Table 1 Physical parameters and their dimensional values or their ranges, taken from ref. 27, 28 and 49

Parameter	Value/range	Description
L	50 μm	Flagellum length
a	100 nm	Axoneme cross-section radius
η	10^{-3} Pa s	Viscosity of surrounding fluid
K	2×10^{3} N m^{-2}	Elastic spring constant of nexin linkers
ρ	2×10^{3} μm^{-1}	Number density of dyneins per length
F_0	1–5 pN	Stall load of dynein on microtubule
F_c	0.5–2.5 pN	Motor unbinding threshold force
v_0	5–7 μm s^{-1}	Zero-load velocity
k_b	17.2 s^{-1}	Binding rate of dyneins
k_u	2.8 s^{-1}	Unbinding rate of dyneins
B_1	1.5×10^{-21} N m^2	Bending rigidity normal to major plane
B_2	$(0.25\text{–}1)B_1$	Bending rigidity in major plane
J	3×10^{-21} N m^2	Twist rigidity
N	9	Number of circumference doublets

$$\begin{aligned}&F_1'' - 2\phi_3'F_2' + (1+\chi)\phi_2'F_3' - \Big(\chi\big(\phi_2'\big)^2+\big(\phi_3'\big)^2\Big)F_1\\ &\quad+\big(\chi\phi_1'\phi_2' - \phi_3''\big)F_2 + (\phi_1'\phi_3' + \phi_2'')F_3 = \mathrm{Sp}^4\partial_t\phi_2,\end{aligned} \tag{14a}$$

$$\begin{aligned}&F_2'' + 2\phi_3'F_1' - (1+\chi)\phi_1'F_3' + (\chi\phi_1'\phi_2' + \phi_3'')F_1\\ &\quad-\Big(\chi\big(\phi_1'\big)^2+\big(\phi_3'\big)^2\Big)F_2 + \big(\phi_2'\phi_3' - \phi_1''\big)F_3 = -\mathrm{Sp}^4\partial_t\phi_1\end{aligned} \tag{14b}$$

$$\begin{aligned}&F_3'' - \frac{1+\chi}{\chi}\phi_2'F_1' + \frac{1+\chi}{\chi}\phi_1'F_2' + \Big(\frac{1}{\chi}\phi_1'\phi_3' - \phi_2''\Big)F_1\\ &\quad+\Big(\phi_1'' + \frac{1}{\chi}\phi_2'\phi_3'\Big)F_2 - \frac{1}{\chi}\Big(\big(\phi_1'\big)^2+\big(\phi_2'\big)^2\Big)F_3 = 0\end{aligned} \tag{14c}$$

$$\begin{aligned}&\mathscr{B}\phi_1'' - (1-\mathscr{J})\phi_2'\phi_3' - F_2 - \mu_K\phi_1\\ &\quad-\mu_a\big(n_1^c + \zeta\big(n_+^c\partial_t\phi_1 + n_2^s\partial_t\phi_2\big)\big) = 0\end{aligned} \tag{14d}$$

$$\begin{aligned}&\phi_2'' + (\mathscr{B}-\mathscr{J})\phi_1'\phi_3' + F_1 - \mu_K\phi_2\\ &\quad-\mu_a\big(n_1^s + \zeta\big(n_2^s\partial_t\phi_1 + n_-^c\partial_t\phi_2\big)\big) = 0\end{aligned} \tag{14e}$$

$$\mathscr{J}\phi_3'' + (1-\mathscr{B})\phi_1'\phi_2' = \frac{\mathrm{Sp}^4a^2}{4\xi_\perp L^2}\partial_t\phi_3, \tag{14f}$$

Table 2 Non-dimensional parameters of computational model (14)

Parameter	Definition	Representative value(s)
Sp	$L\{8\pi\eta\xi_\perp/(B_2\tau_0)\}^{1/4}$	10
μ_K	$2\pi^2Ka^2L^2/(NB_2)$	100
μ_a	$\pi\rho aF_0L^2/B_2$	10^4
ζ	$\pi a/(Nv_0\tau_0)$	0.2
β	$k_b\tau_0$	0.14
α	F_0/F_c	2
χ	$\zeta_\perp/\zeta_\parallel$	2
$\mathscr{B}$	B_1/B_2	1–10
$\mathscr{J}$	J/B_2	2–5

$$\partial_t n = \beta(1-n) - (1-\beta)n\exp\{\alpha W(\theta,s,t)\} + \Lambda\mathcal{N}(\theta,s,t) \quad (14g)$$

$$W = 1 + 2\zeta(\partial_t\phi_1\cos\theta + \partial_t\partial_s\phi_2\sin\theta), \quad (14h)$$

where primes denote partial derivatives with respect to s and we have defined

$$n_k^c = 2\langle n\cos(k\theta)\rangle_\theta, \quad n_k^s = 2\langle n\sin(k\theta)\rangle_\theta, \quad n_\pm^c = n_0^c \pm n_2^c. \quad (15)$$

Here, the notation $\langle g\rangle_\theta = \frac{1}{2\pi}\int_0^{2\pi} g(\theta)\mathrm{d}\theta$ stands for averaging with respect to θ. The quantity $\Lambda\mathcal{N}$ in (14g) represents the derivative of white noise with (dimensionless) variance Λ^2 and is drawn from a normal distribution with zero mean.

These equations are subject to the conditions that the base of the flagellum ($s = 0$) is stationary ($\mathbf{v} = \mathbf{0} \Rightarrow \partial_s\mathbf{F} = 0$) and clamped (without loss of generality, $\phi_i(0,t) = 0$) and that the tip $s = L$ is force- and torque free ($\mathbf{F} = \mathbf{M} = \mathbf{0}$). Separating these conditions into components yields

$$\phi_i = F_i' + \varepsilon_{ijk}\phi_j F_k = 0, \quad \text{at} \quad s = 0, \quad (16a)$$

$$\partial_s\phi_i = F_i = 0 \quad \text{at} \quad s = L, \quad (16b)$$

where ε_{ijk} is the Levi-Civita symbol, subscript indices take values in {1, 2, 3} unless otherwise specified, and we use Einstein's summation convention for repeated indices. The system (14) subject to (16) form the coupled 3D flagellum model, which we solve subject to initial conditions that remain to be specified.

All non-dimensional parameters are listed in Table 2. We distinguish three main non-dimensional parameters: (i) sperm number Sp which is essentially the relative contribution of bending forces to viscous forces, (ii) μ_a which measures activity of dynein motors relative to bending forces, and (iii) bending anisotropy $\mathscr{B} = B_1/B_2$. We focus on the effects of these parameters on the dynamics, while keeping the other quantities fixed.

3 Results and discussion

We solve the system (14) numerically with boundary conditions (16) for $F_i(s,t)$, $\phi_i(s,t)$ and $n(\theta,s,t)$; the numerical implementation is detailed in the ESI.† We use these solutions to integrate (3) and obtain the basis vectors ($\mathbf{e}_1$, $\mathbf{e}_2$, $\mathbf{d}$), which then yields the centerline of the flagellum as $\mathbf{x}(s,t) = \int_0^s \mathbf{d}(u,t)\mathrm{d}u$. We also define a global coordinate system (x,y,z) such that the local and global frames coincide at the base $s = 0$.

In the absence of noise ($\Lambda = 0$), the system (14) and (16) admits the steady-state solution

$$\phi_i^{(\mathrm{eq})} = F_i^{(\mathrm{eq})} = 0, \quad n^{(\mathrm{eq})} = \frac{\beta}{\Gamma}, \quad \text{where} \quad \Gamma = \beta + (1-\beta)e^{\alpha}. \quad (17)$$

This static equilibrium corresponds to a straight flagellum whose centerline coincides with the x axis. Noise in the motor kinetics (14g) perturbs this equilibrium. We study conditions under which these perturbations grow, and the beating patterns that emerge as a consequence. We use the equilibrium solution (17) as the initial condition for the results presented here, though we also explore the sensitivity of the numerical solutions to initial conditions (Section S3, ESI†).

Below, we first discuss beating behaviors observed from numerical solutions. In Section 3.2 we will then develop a linear stability analysis, and obtain an analytic estimate of the threshold for the onset of instability of the static equilibrium state.

3.1 Numerical results

At a fixed Sp, we find from numerical solutions that the static equilibrium is robust to perturbations by noise for sufficiently small motor activity μ_a. For μ_a beyond a Sp-dependent threshold value, the static equilibrium becomes unstable and gives way to periodic beating patterns. Beating patterns persist and change as μ_a is increased further. Some of these features are qualitatively similar to observations in the 2D model of,[28] but in our 3D model, they depend strongly on the new parameters $\mathscr{B} = B_1/B_2$ and $\mathscr{J} = J/B_2$, giving rise to greater variety of beating patterns, which we discuss below.

3.1.1 Isotropic flagella exhibit helical beating. We first consider an isotropic flagellum, that is, the bending stiffness is identical along both bending axes: $B_1 = B_2$ ($\mathscr{B} = 1$). Unsurprisingly, the flagellum relaxes to its static equilibrium for small motor activity μ_a. At sufficiently large μ_a, the flagellum exhibits self-sustained beating, indicated by Fig. 3 for two different combinations of Sp and μ_a. These beating patterns take the form of helical traveling waves that propagate either from tip-to-base (retrograde; Fig. 3A) or from base-to-tip (anterograde; Fig. 3B). The projections of the 3D waveforms onto different planes make the direction of wave propagation more evident, and qualitatively resemble the results of the 2D model developed by ref. 28. The chirality of the helical waves is not inherently biased in the model and is set by noise in the motor kinetics.

Fig. 4 shows the projection of the trajectory traced by the tip of an isotropic flagellum in the yz-plane for different combinations of Sp and μ_a. The tip traces out mostly circular curves in the yz-plane reflecting the bending isotropy in both directions. The beat amplitude (tip trajectories in Fig. 4 are drawn to scale) and the direction of wave propagation depends on Sp and μ_a. The Sp–μ_a space can be divided into four domains depending on the beating dynamics. For low dynein activity (small μ_a) or a stiff flagellum (large Sp), the flagellum relaxes to its equilibrium state over time, as noted earlier (Fig. 4, no move black dots). As μ_a increases past a first threshold at a fixed Sp, the flagellum oscillates spontaneously with waves propagating from tip to base (retrograde) (Fig. 4, red circles in the tip-to-base domain). This first threshold (Fig. 4, black solid curve) is identified as a Hopf bifurcation by a linear stability analysis (detailed later in Section 3.2) and is in good agreement with the computed patterns. Further increasing μ_a at constant Sp yields a second threshold (Fig. 4, red dashed line) where a transition from retrograde (tip-to-base) to anterograde (base-to-tip) (Fig. 4, green circles in the base-to-tip domain) wave propagation occurs. These behaviors are qualitatively similar to the 2D model results of,[28] though they are quantitatively different

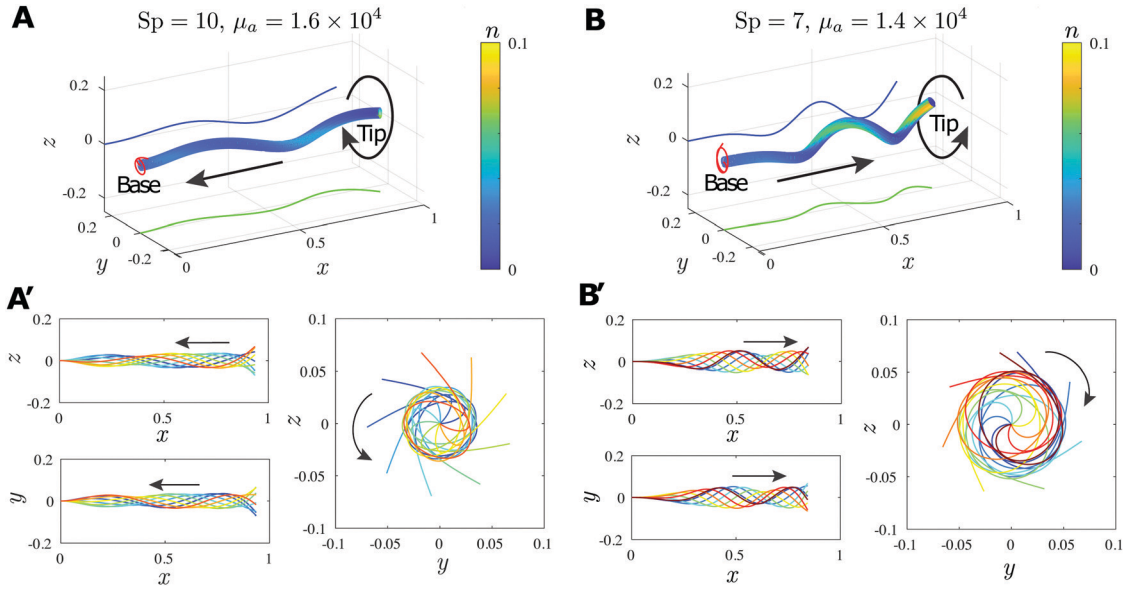

Fig. 3 Beating of isotropic flagellum ($\mathscr{B} = 1$, $\mathscr{J} = 2$) for two specific cases Sp = 10, $\mu_a = 1.6 \times 10^4$ (sub-figures A & A′, also see Movie S1, ESI†) and Sp = 7, $\mu_a = 1.4 \times 10^4$ (sub-figures B & B′, also see Movie S2, ESI†). In sub-figures A and B, the flagellum is depicted as a deformed cylinder in *xyz*-space; blue, green, and red curves are projections of the flagellum's centerline onto *zx*-, *xy*- and *zy*-planes, respectively. Straight black arrows indicate direction of wave propagation: either base-to-tip or tip-to-base. Circular arrows indicate the rotation direction of the tip. Color on the flagellum cylinder shows the density of bound dyneins $n(\theta,s,t)$. Sub-figures A′ & B′ show instantaneous projections of the flagellum centerline onto *zx*-, *xy*- and *zy*-planes in nine consecutive time instants. Curves are colored from blue to red corresponding to the earliest and latest depicted time instants, respectively.

since bending modes in either direction are nonlinearly coupled to each other in our 3D model.

We observe that the beating amplitude (represented by the radii of the circular tip trajectories in Fig. 4) increases with μ_a in the tip-to-base regime after passing the stability threshold, for each Sp. Crossing the second threshold between the tip-to-base and base-to-tip domains causes a drop in amplitude, and then a gradual increase again with increasing μ_a.

Finally, for the combination of small Sp and large μ_a (very flexible flagella with high motor activity), we find that the beating pattern is sensitive to initial conditions. Within this "initial condition (IC)-sensitive" domain, applying different initial conditions (for example, initially stretching or compressing the flagellum) leads to either base-to-tip or tip-to-base beating dynamics that are stable against noise; see Fig. S1 (ESI†). This region also contains a few parameter combinations with a large-amplitude dynamics yet without a clear pattern (shown by the light red colors in Fig. 4). We speculate that these may correspond to either another instability or long-lived transients, though we do not investigate these in detail. Comparing Fig. 4 with Fig. S1 (ESI†) makes it clear that outside the IC sensitive domain, beating patterns are robust to initial conditions, except for a few close to the transition thresholds. In most cases, the beating occurs as isotropic helical waves.

3.1.2 Anisotropic flagella may lead to either planar or 3D oscillations. Next, we consider an anisotropic flagellum with $\mathscr{B} = B_1/B_2 > 1$, which models the effect of the 5–6 bridge as differential bending resistance. We study $\mathscr{B} = B_1/B_2 = 2, 3, 5, 10$, with fixed twist modulus $\mathscr{J} = 5$ (Fig. 5); note that ref. 43 estimates $\mathscr{B} \approx 2.6$. Similar to an isotropic flagellum, small μ_a and large Sp result in stable no move states without beating (Fig. 5, black dots). Across the first threshold, the equilibrium state becomes unstable *via* a Hopf bifurcation. However, this time, the instability manifests as periodic planar (and not 3D) oscillations with tip-to-base waves in the single plane corresponding to the softer axis (Fig. 5, red lines). This is perhaps surprising as the bending coefficients B_1 and B_2, though unequal, are of the same order of magnitude. Linear stability analysis (Section 3.2) rationalizes this observation by showing that unstable modes along the soft axis (B_2) are triggered for smaller activity than the stiff axis (B_1). This is in contrast with the isotropic case, where both planes of beating become simultaneously unstable and result in a 3D instability.

On further increasing μ_a while keeping Sp fixed, we observe two other thresholds: a 2D-to-3D transition threshold (Fig. 5, blue solid curves) and a retrograde-to-anterograde transition threshold (Fig. 5, red dashed curves). From our simulations, it appears that the order in which these two thresholds emerge depends on the bending stiffness ratio $\mathscr{B}$.

For smaller $\mathscr{B}$ values, the 2D-to-3D threshold shows up ahead of the retrograde-to-anterograde threshold (Fig. 5A), dividing the domain into a 2D retrograde domain (red lines), a 3D retrograde domain (red closed curves), and a 3D anterograde domain (green curves). Many of the trajectories in 3D anterograde domain show chaotic patterns (*e.g.* light green in Fig. 5A) and may also be sensitive to initial conditions; we do not discuss them in detail.

For intermediate values of $\mathscr{B}$, the 2D-to-3D threshold mostly overlaps with the retrograde-to-anterograde threshold (Fig. 5B), leading to a very small 2D anterograde domain (green lines). As $\mathscr{B}$ increases further, the 2D-to-3D threshold shows up after the

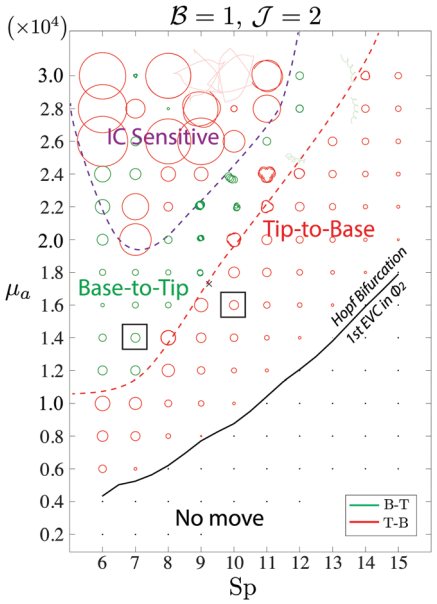

Fig. 4 Phase diagram for isotropic flagellum with $\mathscr{B} = 1$ and $\mathscr{J} = 2$. At each Sp and μ_a, the trajectory of the flagellum tip, projected on the yz-plane, is depicted around point (Sp, μ_a). All trajectories are drawn to scale. Black solid line separates regions in (Sp, μ_a) of stability and instability of the trivial solution corresponding to the straight flagellum. Trajectories above the solid line are oscillatory with the amplitude increasing away from the solid line, thus, the bifurcation when one crosses the solid line from below is the supercritical Hopf bifurcation. For trajectories above the solid line, green and red colors indicate base-to-tip (B–T) and tip-to-base (T–B) directions of wave propagation, respectively. Trajectories with large amplitudes but without a clear pattern are shown by light (red) colors. Trajectories enclosed by squares are considered in more detail in Fig. 3.

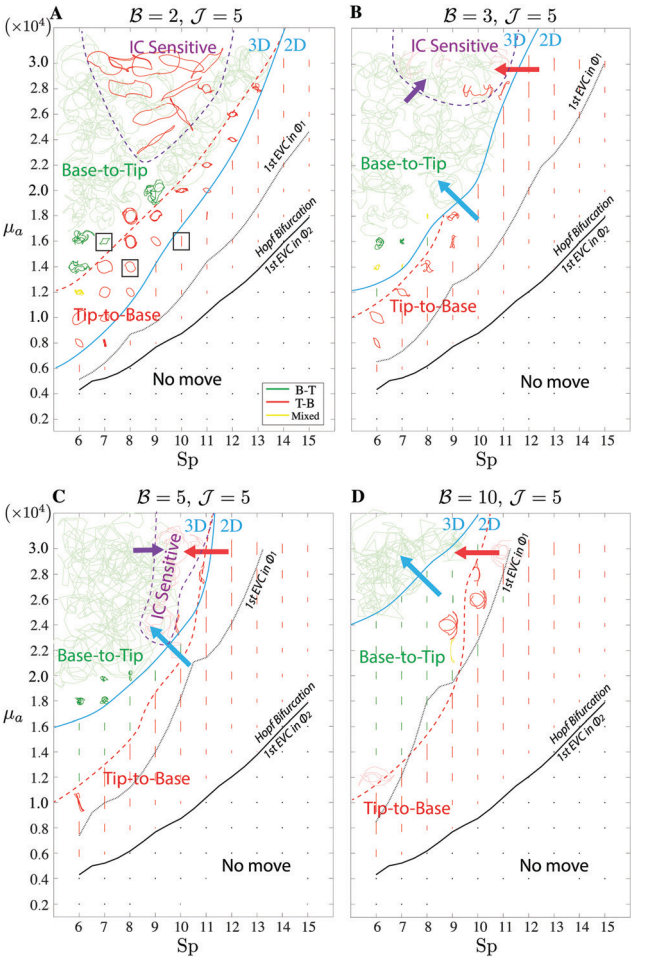

Fig. 5 Phase diagram for anisotropic flagellum with $\mathscr{J} = J/B_2 = 5$, $\mathscr{B} = B_1/B_2 = 2, 3, 5, 10$. Each sub-figure is analogous to Fig. 4: tip trajectories are projected on yz-plane for various values of (Sp, μ_a), and color indicates wave propagation direction (red for retrograde and green for anterograde waves). Yellow trajectories do not exhibit a clear wave direction, and dots represents relaxation to the equilibrium state. Black solid/dotted lines show where the leading eigenvalue crossing (EVC) the imaginary axis of the soft/stiff axis (Section 3.2); the black solid line indicates the Hopf bifurcation. Blue solid lines separate 2D planar beating and 3D beating. Purple dashed lines enclose the IC sensitive domains, where beating dynamics may depend on the choice of initial conditions. Arrows indicate the change in the thresholds as $\mathscr{B}$ increases. Boxed trajectories are shown in more detail in Fig. 6.

retrograde-to-anterograde threshold (Fig. 5C and D), leading to an expanding 2D anterograde domain (green lines). In an anisotropic flagellum, we also observe an IC sensitive domain, where beating can be either chaotic anterograde (light green curves) or retrograde showing certain large-amplitude patterns (red curves).

At larger values of $\mathscr{B}$, 2D anterograde beating occurs over a wider part of the parameter space (Fig. 5C and D, green arrows). This should be expected on physical grounds since for large $\mathscr{B}$, it becomes harder to bend in the stiffer direction, leading to dynamics that resemble those of a 2D flagellum. Increasing $\mathscr{B}$ also appears to cause a slight expansion of the retrograde domain (Fig. 5, red arrows) and a shrinking of the IC sensitive domain (Fig. 5, purple arrows).

We show an example of beating dynamics in Fig. 6, corresponding to the boxed trajectories in Fig. 5A for $\mathscr{B} = 2$, $\mathscr{J} = 5$. As evident from the 2D projections of the 3D flagellum waveforms, the shapes of the patterns, the relative amplitudes along the two bending planes, and the wave direction are sensitive to choice of parameters.

Our model thus shows that even a modest anisotropy in the bending stiffness leads to a rich variety of beating patterns that are qualitatively distinct from those of the isotropic case. In particular, this includes planar (or nearly planar) beating behaviors in the principal bending plane, with both retrograde and anterograde waves. Such quasi-planar beating is robust across a range of parameters and emerges spontaneously despite the 3D beating machinery of the model. Some of the simulated patterns are clearly non-planar but continue to show signatures of a dominant beating plane, especially for not-too-large $\mathscr{B}$ and shorter flagella corresponding to smaller Sp (Fig. 5 and 6). Qualitatively similar beating was recently observed in *Chlamydomonas*.[32]

The planar retrograde trajectories just above the Hopf bifurcation can be understood in terms of dynamics along the soft axis being linearly unstable, while those along the stiff axis remain linearly stable. This is evident from a linear stability analysis (Section 3.2) which yields the Hopf bifurcation curves for beating along the soft and stiff axes (black curves in Fig. 5). We

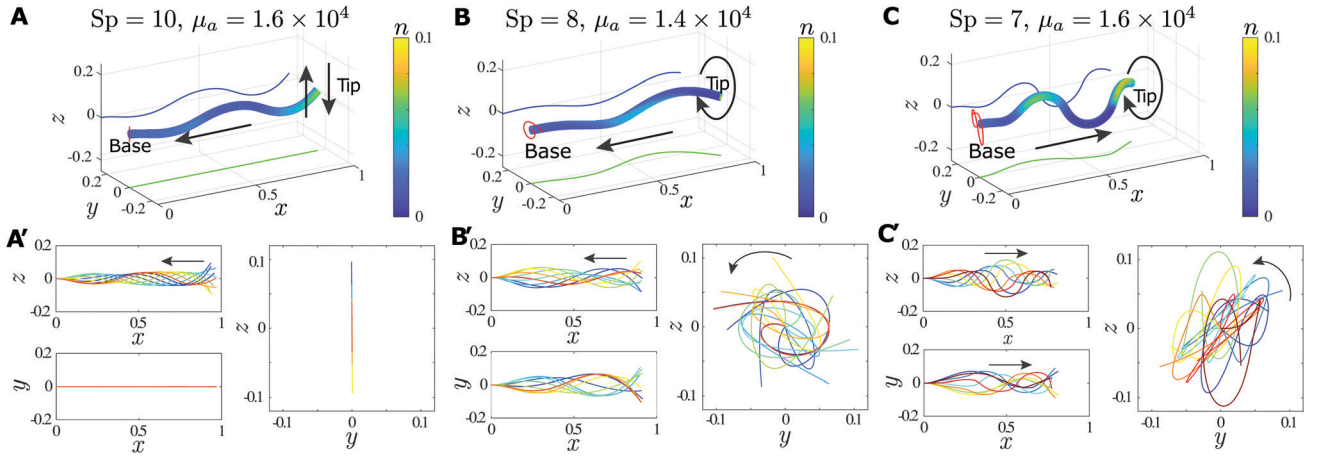

Fig. 6 Beating of anisotropic flagellum ($\mathscr{B} = 2$, $\mathscr{J} = 5$) for three specific cases with (A and A′) Sp = 10, $\mu_a = 1.6 \times 10^4$, 2D retrograde, also see Movie S3 (ESI†). (B and B′) Sp = 8, $\mu_a = 1.4 \times 10^4$, 3D retrograde, also see Movie S4 (ESI†). (C and C′) Sp = 7, $\mu_a = 1.6 \times 10^4$, 3D anterograde, also see Movie S5 (ESI†). Notations are the same as in Fig. 3.

note that the 2D-to-3D transition threshold curve is well above the curve of the leading eigenvalue crossing the imaginary axis in the stiff axis (black dotted curves in Fig. 5), and so conclude that this transition is a feature of nonlinearities in the model. In fact, many trajectories above the 1st EVC in ϕ_1 curve but below the 2D-to-3D transition threshold depart from the initial condition by bending about both the soft and the stiff axes, but ultimately exhibit beating patterns where bending about the soft axis (nonlinearly) suppresses bending about the stiff axis.

We also consider the effect of the twist modulus $\mathscr{J}$. For isotropic flagella, the twist relaxes exponentially to zero (up to noise determined by motor kinetics) and the beating becomes independent of $\mathscr{J}$, *cf.* (14). By contrast, anisotropic flagella beat with a finite twist, with larger $\mathscr{J}$ leading to less twisting. Overall, we find that $\mathscr{J}$ has a relatively small impact on the flagellum beating dynamics and exerts a modest influence on the location of the phase boundaries; see Section S4 and Fig. S2 (ESI†).

3.2 Instability threshold for the equilibrium state

3.2.1 Linear stability analysis. We now identify the threshold when the static equilibrium state (17) becomes unstable using linear stability analysis, following the workflow in ref. 27. We linearize (14) about the base state to obtain

$$\partial_t n = \beta - \Gamma n - 2\zeta\alpha\beta\left(1 - \frac{\beta}{\Gamma}\right)(\partial_t\phi_1 \cos\theta + \partial_t\phi_2 \sin\theta), \quad (18a)$$

$$[F_1,\ F_2,\ F_3]'' = \mathrm{Sp}^4\,[\phi_1,\ -\phi_2, 0] \quad (18b)$$

$$\mathscr{B}\phi_1'' - F_2 - \mu_K\phi_1 - \mu_a\left(n_1^c + 2\zeta n^{(\mathrm{eq})}\partial_t\phi_1\right) = 0, \quad (18c)$$

$$\phi_2'' + F_1 - \mu_K\phi_2 - \mu_a\left(n_1^s + 2\zeta n^{(\mathrm{eq})}\partial_t\phi_2\right) = 0, \quad (18d)$$

$$\mathscr{J}\phi_3'' = \frac{\mathrm{Sp}^4 a^2}{4\xi_\perp L^2}\partial_t\phi_3, \quad (18e)$$

where we recall that $\Gamma = \beta + (1 - \beta)e^{\alpha}$; see (17), Table 2. Linearizing the boundary conditions yields

$$\phi_i|_{s=0} = F_i'|_{s=0} = \phi_i|_{s=1} = F_i|_{s=1} = 0. \quad (19)$$

Eqn (18a) admits solutions of the form $n(\theta,s,t) = n_0^c(s,t) + n_1^c(s,t)\cos\theta + n_1^s(s,t)\sin\theta$, which separate into independent equations for the Fourier modes.

For each dynamical variable $f(s,t)$, we seek eigensolutions $f(s,t) = \tilde{f}(s)e^{\sigma t}$. We substitute this ansatz into the linearized equations and eliminate the force components by taking two derivatives of (18c) and (18d) and utilizing (18a) and (18b), to obtain

$$\mathscr{B}\tilde{\phi}_1'''' - \Phi(\sigma)\tilde{\phi}_1'' + \mathrm{Sp}^4\sigma\tilde{\phi}_1 = 0, \quad (20a)$$

$$\tilde{\phi}_2'''' - \Phi(\sigma)\tilde{\phi}_2'' + \mathrm{Sp}^4\sigma\tilde{\phi}_2 = 0, \quad (20b)$$

$$\mathscr{J}\tilde{\phi}_3'' - \frac{\mathrm{Sp}^4 a^2}{4\xi_\perp L^2}\sigma\tilde{\phi}_3 = 0, \quad (20c)$$

where we have defined

$$\Phi(\sigma) = \mu_K + 2\mu_a\zeta\frac{\beta}{\Gamma}\sigma\left(1 - \left(1 - \frac{\beta}{\Gamma}\right)\frac{\alpha\Gamma}{\sigma + \Gamma}\right). \quad (21)$$

The boundary conditions reduce to (using the notation $\mathscr{B}_1 = 1$ and $\mathscr{B}_2 = \mathscr{B}$)

$$\tilde{\phi}_\ell = B_\ell\tilde{\phi}_\ell''' - \Phi(\sigma)\tilde{\phi}_\ell' = 0 \quad (\ell = 1,2), \quad \text{at} \quad s = 0,\ s = 1. \quad (22)$$

We observe that the dynamics for $\phi_{1,2}$ closely resemble the linearized 2D model of ref. 27.

To analyze the instability threshold, we are interested in σ with $\mathrm{Re}\,\sigma \geq 0$ such that the problem (20a)–(20c) with boundary conditions (22) possesses a non-trivial solution $(\phi_1,\ \phi_2,\ \phi_3)$. We observe that the linearized dynamics for the three rotation angles are decoupled. The twist angle admits solutions $\tilde{\phi}_3 = \sin\left(\frac{(2k+1)\pi}{2}s\right)$ with $k = 0, 1, 2, \ldots$, corresponding to a

negative growth rate $\sigma = -4\xi_\perp L^2 \mathscr{J}/(\mathrm{Sp}^4 a^2)$. The equilibrium state is therefore linearly stable to twist.

The eqn (20a) and (20b) govern the stability of $\phi_{1,2}$. We look for solutions $\tilde{\phi}_\ell = \sum_{j=1}^{4} X_j^{(\ell)} e^{p_j^{(\ell)} s}$, with $\ell = 1, 2$, where the $X_j^{(\ell)}$ are constants and $p_j^{(\ell)}$ are the distinct roots of the characteristic equations for (20a) and (20b), $\mathscr{B}_\ell p^4 - \Phi(\sigma)p^2 + \mathrm{Sp}^4\sigma = 0$. Applying boundary conditions (22a), we find that nontrivial solutions exist only when

$$\det \mathscr{P}^{(\ell)} = \det\left[\mathbf{P}_1^{(\ell)}\mathbf{P}_2^{(\ell)}\mathbf{P}_3^{(\ell)}\mathbf{P}_4^{(\ell)}\right] = 0,$$

with

$$\mathbf{P}_j^{(\ell)} = \begin{bmatrix} 1 \\ p_j^{(\ell)} e^{p_j^{(\ell)}} \\ \left(\mathscr{B}_\ell (p_j^{(\ell)})^2 - \Phi\right) p_j^{(\ell)} \\ \left(\mathscr{B}_\ell (p_j^{(\ell)})^2 - \Phi\right) e^{p_j^{(\ell)}} \end{bmatrix}, \quad \ell = 1, 2. \tag{23}$$

In summary, σ is an eigenvalue of the linearized problem (18) if roots of characteristic equation for either (20a) or (20b) satisfy (23).

In Fig. 7, we depict contours of $\ln|\det \mathscr{P}^{(\ell)}(\sigma)|$ for $\ell = 1, 2$ as functions of the complex variable σ, with two different choices of problem parameters Sp, $\mathscr{J}$, and μ_a. Eigenvalues σ are identified by small red circles and correspond to $\det \mathscr{P}^{(\ell)}(\sigma) = 0$. Given values of Sp, $\mathscr{J}$, and μ_a the system is linearly stable if all eigenvalues σ for both $\ell = 1$ and $\ell = 2$ are to the left of the imaginary axis $\mathrm{Re}\,\sigma = 0$. When parameters are varied and the rightmost value of σ crosses the imaginary axis from left to right, the equilibrium solution transitions from stable to unstable state. In Fig. 4 and 5 we depict the curve that separates stable and unstable regions in parameter plane (Sp, μ_a) (the black solid curve). For $B_1 = B_2$, bending modes in both directions become simultaneously unstable, leading to 3D beating patterns. However, for $B_1 > B_2$, the most unstable eigenmodes of (20b) lie to the right of the most unstable modes of (20a). Thus the instability of an anisotropic flagellum is initiated as a 2D eigenmode oscillating about the soft bending axis, independent of $\mathscr{B}$, as is observed in the simulations; see Section 3.1.2, Fig. 5.

3.2.2 Analytic approximation of the linear stability threshold. To gain analytic insight into the onset of instability, we focus on the linearized dynamics of ϕ_2. The characteristic equation of (20b), $(p^{(2)})^4 - \Phi(p^{(2)})^2 + \mathrm{Sp}^4\sigma = 0$, admits solutions $p_1^{(2)} = -p_3^{(2)} = \sqrt{\frac{\Phi + \sqrt{\Phi^2 - 4\mathrm{Sp}^4\sigma}}{2}}$, $p_2^{(2)} = -p_4^{(2)} = \sqrt{\frac{\Phi - \sqrt{\Phi^2 - 4\mathrm{Sp}^4\sigma}}{2}}$. Substituting these solutions into (23), we find (using Mathematica) that the growth rate σ satisfies

$$\Phi^2 - \Phi p_1^{(2)} p_2^{(2)} \tanh p_1^{(2)} \tanh p_2^{(2)} - 2\mathrm{Sp}^2\sigma(1 + \mathrm{sech} p_1^{(2)} \mathrm{sech} p_2^{(2)}) = 0. \tag{24}$$

We now seek solutions of (24) in the limit where spatial mode exponents $p_1^{(2)}$ and $p_2^{(2)}$ have asymptotically large real parts, which will turn out to govern the instability of the entire system. In this limit, (24) becomes $\Phi^2 - \Phi p_1^{(2)} p_2^{(2)} - 2\mathrm{Sp}^2\sigma \approx 0$. Substituting the expressions for $p_{1,2}^{(2)}$ into this approximate

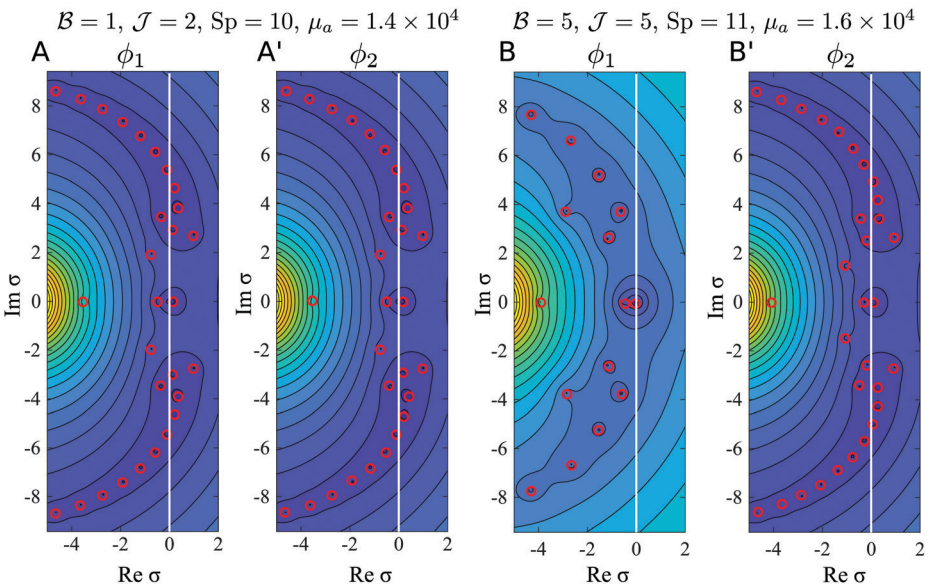

Fig. 7 Eigenvalues of the linearized problem (18a)–(18e). For two cases (Sp = 10, $\mathscr{J}$ = 2, $\mu_a = 1.4 \times 10^4$) (sub-figures A & A′) and (Sp = 11, $\mathscr{J}$ = 5, $\mu_a = 1.6 \times 10^4$) (sub-figures B & B′), color-plots for $\log|\det \mathscr{P}^{(1)}|$ (sub-figures A & B) and $\log|\det \mathscr{P}^{(2)}|$ (sub-figures A′ & B′) as functions of complex variable σ are depicted; yellow color corresponds to small magnitudes whereas dark blue color corresponds to large magnitudes. Peaks are identified numerically and indicated by red circles centers of which are eigenvalues obtained from (20a) (sub-figures A & B) and (20b) (sub-figures A′ & B′). Vertical white line depicts imaginary axis $\mathrm{Re}\,\sigma = 0$.

equation yields [see ESI†]

$$\Phi \approx -\mathrm{Sp}^2\sqrt{\sigma}, \tag{25}$$

which, when combined with (21), forms an implicit equation for σ. The threshold of instability is determined by σ crossing the imaginary axis, so we look for imaginary solutions $\sigma = i\Gamma\omega$, where ω is a rescaled (real) oscillation frequency to be found. Substituting into (25), and separating into real and imaginary parts yields

$$\mathscr{K} = \frac{\mu_K}{2\mu_a\beta\zeta} = \frac{\omega(\gamma\omega - \gamma + \omega^2 + 1)}{\omega^2 + 1}, \tag{26a}$$

$$\mathscr{G} = \frac{\mathrm{Sp}^2\Gamma^{1/2}}{2\mu_a\beta\zeta} = \frac{\sqrt{2\omega}(\gamma - \omega^2 - 1)}{\omega^2 + 1}, \tag{26b}$$

where $\gamma = \alpha(1 - \beta/\Gamma)$ is a parameter that depends on the motor kinetics. This defines a curve in $\mathscr{G} - \mathscr{K}$ space (parametrized by ω) corresponding to the onset of instability of modes with large spatial exponents. A judicious linearization of (26a) [see ESI†], after casting in terms of μ_a and Sp, yields a closed-form approximation for the threshold for instability

$$\mu_a \approx \frac{\mu_K + D\Gamma^{1/2}\mathrm{Sp}^2}{2C\beta\zeta}, \tag{27}$$

Here, C and D are analytic functions of γ [see ESI†]; for the parameters in Table 2, $\gamma \approx 1.96$, yielding $C \approx 0.96$ and $D \approx 1.56$.

Fig. 8 shows that the relation (27) provides an excellent prediction of the stability of the system for the parameter range studied. We note that (27) describes the instability threshold of modes with large spatial exponents $\mathrm{Re}[p_1,p_1] \gg 1$. These modes appear to also have the fastest growth rates and control the linear stability of the entire system. The analysis reveals that unstable modes at the onset of instability have dimensionless wavelengths that scale as Sp^{-1} (dimensional wavelength $\propto (B_2\tau_0/(\xi_\perp\eta))^{1/4}$), associated with dimensionless forces $F_{1,2}$ scaling as Sp^2 (dimensional force scale $\propto (B_2\eta\xi_\perp/\tau_0)^{1/2}$). It remains to be seen how well these scaling relations persist far away from the stability threshold, and whether they provide insight into the nonlinear dynamical regime.

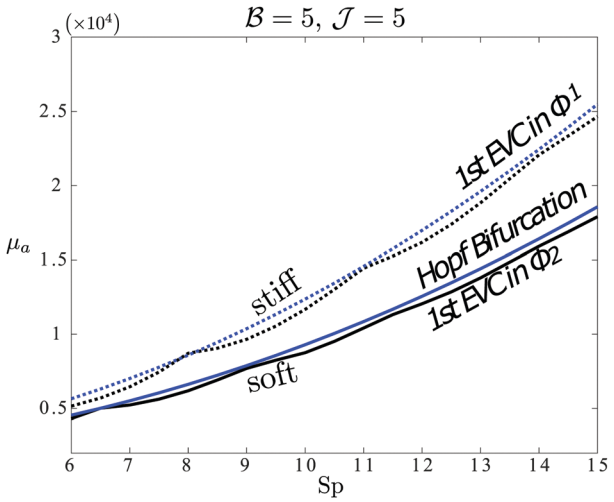

Fig. 8 Comparison of the first eigenvalue crossing (EVC) between the numerical simulations and the analytical solution, with $\mathscr{B} = 5$, $\mathscr{J} = 5$. Black solid and dotted lines are from numerical solutions of the eigenvalue problem, blue solid and dashed lines are from (27). The lower threshold, corresponding to the soft axis, governs the linear stability of the system.

4 Conclusions

In this work, we developed a novel 3D model of eukaryotic flagellum capturing both bending and twist of axoneme structure tied into dynein motor kinetics. Our main focus is to explore the possible options of a single flagellum beating dynamics out of a 3D machinery. In particular, we studied the effects of a differential resistance to bending in and orthogonal to the principal bending plane, which occurs due to the internal structure of the axoneme. Computational results show that self-sustained beating modes are excited after crossing a Hopf bifurcation that occurs at sufficiently high motor activity. We find that an isotropic flagellum, which has identical bending stiffness both bending axes, beats by propagating helical waves. However, for an anisotropic flagellum, even a small bias in bending stiffness can lead to a wide variety of beating patterns that include both planar and non-planar beating patterns. Simulations also find that the direction of the beating waves generated are always retrograde (tip-to-base) after the motor activity μ_a is sufficient to trigger the Hopf bifurcation, while a further increase in activity will lead to the transition from retrograde to anterograde (base-to-tip) beating. Meanwhile, in an anisotropic flagellum, depending on the bending stiffness ratio $\mathscr{B}$, another transition from 2D to 3D beating may also emerge, leading to different combinations of retrograde/anterograde and 2D/3D beating behaviors.

Computational results show that very flexible flagella with large motor activity (small Sp and large μ_a) may result in domains sensitive to initial conditions or exhibiting chaotic patterns, both associated with large amplitude chaotic beating. The present model is based on the assumption that internal sliding forces are generated by small deformations. Further development of the model to account for nonlinearities large-amplitude sliding may provide better insights in these behaviors. Linear stability analysis provides insight into the no-move-to-beating threshold, showing that beating is initiated along the softer axis. An approximate analysis identifies that the most unstable modes of the dynamics have the shortest allowable wavelengths, set by a combination of the bending rigidity, fluid viscosity and the motor kinetic timescale, but only weakly dependent on the length of the flagellum.

Taking into account flagella dynamics is important in elucidating swimming strategies of various types of biological microswimmers as well as their impact on macroscopic properties of their habitat, see *e.g.* ref. 50. The 3D model developed here shows promise in understanding experimentally observed beating patterns[30,32] and their relation to motor kinetics.

Though here we consider only eukaryotic flagella rigidly attached (clamped) to an immobilized surface, our computational model can be further developed to describe fully mobile

microswimmers. This may include situations where one or more active flagella propel a head of a finite size through fluid. It is noteworthy that 2D flagellum models that are set free to swim in this way exhibit beating patterns that are qualitatively different from their clamped analogs. It is pertinent to ask how our 3D flagellum model including bending anisotropy and twist will be modified when similarly relaxed to a free-swimming state. Such a model may deepen our understanding of the swimming dynamics of eukaryotic microorganisms.

Author contributions

All authors conceptualized the project, developed the methods, analyzed the model results, and wrote the manuscript.

Conflicts of interest

There are no conflicts to declare.

Acknowledgements

The authors thank Dr. Brato Chakrabarti, Dr. David Saintillan and Dr. Kirsty Wan for stimulating conversations. B. R. acknowledges partial support from the NSF (CBET-2143943). Computations were performed using the computer clusters and data storage resources of the HPCC at UC Riverside, which were funded by grants from the NSF (MRI-1429826) and the NIH (1S10OD016290-01A1).

Notes and references

1 M. Sleigh, J. Blake and N. Liron, *Am. Rev. Respir. Dis.*, 1988, **137**, 726–741.
2 J. Blake, M. Sleigh and N. Liron, *Cilia, Mucus, and Mucociliary Interactions*, Dekker, New York, 1998, pp. 119–126.
3 D. R. Brumley, K. Y. Wan, M. Polin and R. E. Goldstein, *eLife*, 2014, **3**, e02750.
4 Y. Man and E. Kanso, *Phys. Rev. Lett.*, 2020, **125**, 148101.
5 M. L. Byron, D. W. Murphy, K. Katija, A. P. Hoover, J. Daniels, K. Garayev, D. Takagi, E. Kanso, B. J. Gemmell, M. Ruszczyk and A. Santhanakrishnan, *Integr. Comp. Biol.*, 2021, **61**, 1674–1688.
6 B. Chakrabarti, S. Fürthauer and M. J. Shelley, *Proc. Natl. Acad. Sci. U. S. A.*, 2022, **119**(4), e2113539119.
7 I. R. Gibbons, *J. Cell Biol.*, 1981, **91**, 107–124.
8 H. Hoops and G. Witman, *J. Cell Biol.*, 1983, **97**, 902–908.
9 C. D. Silflow and P. A. Lefebvre, *Plant Physiol.*, 2001, **127**, 1500–1507.
10 I. Manton and B. Clarke, *J. Exp. Bot.*, 1952, **3**, 265–275.
11 P. Satir, D. Mitchell and G. Jékely, *Curr. Top. Dev. Biol.*, 2008, **85**, 63–82.
12 R. Linck, H. Chemes and D. Albertini, *J. Assist. Reprod. Genet.*, 2016, **33**, 141–156.
13 H. Lodish, A. Berk, C. Kaiser, M. Krieger, M. Scott, A. Bretscher, H. Ploegh and P. Matsudaira, *Molecular Cell Biology*, Macmillan, 2008.
14 P. Yang, D. Diener, C. Yang, T. Kohno, G. Pazour, J. Dienes, N. Agrin, S. King, W. Sale, R. Kamiya and J. Rosenbaum, *J. Cell Sci.*, 2006, **119**, 1165–1174.
15 I. R. Gibbons and A. J. Rowe, *Science*, 1965, **149**, 424–426.
16 C. Brokaw, *J. Exp. Biol.*, 1971, **55**, 289–304.
17 M. Hines and J. Blum, *Biophys. J.*, 1978, **23**, 41–57.
18 P. Sartori, V. Geyer, A. Scholich, F. Jülicher and J. Howard, *eLife*, 2016, **5**, e13258.
19 C. Lindemann, *J. Theor. Biol.*, 1994, **168**, 175–189.
20 R. Dillon and L. Fauci, *J. Theor. Biol.*, 2000, **207**, 415–430.
21 C. Brokaw, *Proc. Natl. Acad. Sci. U. S. A.*, 1975, **72**, 3102–3106.
22 F. Jülicher and F. Prost, *Phys. Rev. Lett.*, 1997, **78**, 4510.
23 S. Camalet, F. Jülicher and J. Prost, *Phys. Rev. Lett.*, 1999, **82**, 1590.
24 I. Riedel-Kruse, A. Hilfinger, J. Howard and F. Jülicher, *HFSP J.*, 2007, **1**, 192–208.
25 T. Mitchison and H. Mitchison, *Nature*, 2010, **463**, 308–309.
26 P. Satir and T. Matsuoka, *Cell Motil. Cytoskeleton*, 1989, **14**, 345–358.
27 D. Oriola, H. Gadêlha and J. Casademunt, *R. Soc. Open Sci.*, 2017, **4**, 160698.
28 B. Chakrabarti and D. Saintillan, *Phys. Rev. Fluids*, 2019, **4**, 043102.
29 Y. Man, F. Ling and E. Kanso, *Philos. Trans. R. Soc., B*, 2020, **375**, 20190157.
30 T.-W. Su, L. Xue and A. Ozcan, *Proc. Natl. Acad. Sci. U. S. A.*, 2012, **109**, 16018–16022.
31 T.-W. Su, I. Choi, J. Feng, K. Huang, E. McLeod and A. Ozcan, *Sci. Rep.*, 2013, **3**, 1–8.
32 D. Cortese and K. Y. Wan, *Phys. Rev. Lett.*, 2021, **126**, 088003.
33 A. Hilfinger and F. Jülicher, *Phys. Biol.*, 2008, **5**, 016003.
34 J. Simons, L. Fauci and R. Cortez, *J. Biomech.*, 2015, **48**, 1639–1651.
35 B. Audoly and Y. Pomeau, *Elasticity and Geometry: From Hair curls to the Non-linear Response of Shells*, Oxford University Press, 2010.
36 M. Rubin, *Cosserat Theories: Shells, Rods and Points*, Springer Science & Business Media, 2013, vol. 79.
37 J. Gray and G. Hancock, *J. Exp. Biol.*, 1955, **32**, 802–814.
38 G. Batchelor, *J. Fluid Mech.*, 1970, **44**, 419–440.
39 J. Lighthill, *SIAM Rev.*, 1976, **18**, 161–230.
40 E. Lauga and T. Powers, *Rep. Prog. Phys.*, 2009, **72**, 096601.
41 L. Leal, *Advanced Transport Phenomena: Fluid Mechanics and Convective Transport Processes*, Cambridge University Press, 2007.
42 S. Childress, *Mechanics of Swimming and Flying*, Cambridge University Press, 1981, vol. 2.
43 C. Lindemann and K. Lesich, *Cytoskeleton*, 2016, **73**, 652–669.
44 W. Sale and P. Satir, *Proc. Natl. Acad. Sci. U. S. A.*, 1977, **74**, 2045–2049.
45 M. Holwill and P. Satir, *Cell Motil. Cytoskeleton*, 1994, **27**, 287–298.
46 S. Hayashi and C. Shingyoji, *J. Cell Sci.*, 2008, **121**, 2833–2843.
47 C. Lindemann and K. Lesich, *J. Cell Sci.*, 2010, **123**, 519–528.
48 M. Shelley, *Annu. Rev. Fluid Mech.*, 2016, **48**, 487–506.
49 P. Bayly and K. Wilson, *Biophys. J.*, 2014, **107**, 1756.
50 M. Potomkin, M. Tournus, L. Berlyand and I. Aranson, *J. R. Soc., Interface*, 2017, **14**, 20161031.

